

Dynamic phase diagram of plastically deformed amorphous solids at finite temperature

Daniel Korchiński* and Jörg Rottler

*Department of Physics and Astronomy and Stewart Blusson Quantum Matter Institute,
University of British Columbia, Vancouver BC V6T 1Z1, Canada*

The yielding transition that occurs in amorphous solids under athermal quasistatic deformation has been the subject of many theoretical and computational studies. Here, we extend this analysis to include thermal effects at finite shear rate, focusing on how temperature alters avalanches. We derive a nonequilibrium phase diagram capturing how temperature and strain rate effects compete, when avalanches overlap, and whether finite-size effects dominate over temperature effects. The predictions are tested through simulations of an elastoplastic model in two dimensions and in a mean-field approximation. We find a new scaling for temperature-dependent softening in the low-strain rate regime when avalanches do not overlap, and a temperature-dependent Herschel-Bulkley exponent in the high strain rate regime when avalanches do overlap.

I. INTRODUCTION

Amorphous solids are materials that, like fluids, lack long-range order on the constituent particle scale, yet are solid at rest. When deformed slowly, these solids respond, first elastically and then once a critical stress is achieved, plastically [1, 2]. This response can be either brittle, with system spanning shear bands, or ductile, with homogeneous plasticity [3–5]. Ductile plastic flow is “jerky”, with periods of elastic stress-loading punctuated by short bursts of stress-releasing plastic rearrangement. These rearrangements can be decomposed into individual shear-transformations (STs), regions of plastic deformation typically involving a few tens of particles [6–8]. Each ST causes a rearrangement that locally relieves stress, while inducing a long-range quadrupolar stress-field [8–11] that can trigger further STs in an avalanche. In the flowing state, in absence of flow inhomogeneities, the hallmarks of a dynamical phase transition emerge: avalanches are scale-free, with non-trivial critical exponents [12–20].

Much theoretical attention has been paid to the ductile yielding transition in the athermal and quasistatic (AQS) limit [12, 16, 19–22]. This limit is appropriate when the plastic ST timescale τ , over which rearrangements occur, is much smaller than the periods of elastic loading (set by the driving rate) and the timescale of thermally triggered STs. When driving rate competes with the timescale of plastic rearrangements, rheological effects begin to alter the phase-transition picture [23–26]. For systems where the constituent particles are large and Brownian motion small (e.g. foams, emulsions, dense suspensions, etc.) thermal effects can be safely neglected [27]. However, for systems with smaller particles or higher temperatures (e.g. metallic glasses close to the glass-transition temperature T_g), thermal effects begin to play a role.

Thermal history can affect whether yielding is brittle or ductile [28–31]. Specifically in ductile steady-

state flow, the competition of thermal and driving-rate timescales can bring new rheological effects into play, as shown for instance in the molecular dynamics study of Karmarkar et al. [32]. If driving rates $\dot{\gamma}$ are increased, so that the loading time between avalanches becomes so short as to be comparable to the duration of the average avalanche $\langle t \rangle_{av}$, avalanches begin to overlap [32]. These overlapping avalanches destroy the anomalous stress-fluctuations of the AQS yielding transition, and the flow stress Σ rises above the athermal critical stress Σ_c according to the Herschel-Bulkley law [12, 33, 34],

$$\Sigma(T = 0, \dot{\gamma}) = \Sigma_c + A\dot{\gamma}^n. \quad (1)$$

Computational studies of thermal activation effects on the yielding transition have been conducted with molecular dynamics simulations of glass formers [35] and more recently with mesoscale elastoplastic models (EPM) [36–38]. In overdamped systems in general, the flow stress decreases with temperature and increases with driving rate. Recent EPM studies have mostly focused on the scaling of the flow stress and have proposed that it takes a scaling form (in analogy with the depinning transition [39])

$$\dot{\gamma} \sim T^\psi f\left(\frac{\Sigma(T, \dot{\gamma}) - \Sigma(T = 0, \dot{\gamma} = 0)}{T^{1/\alpha}}\right) \quad (2)$$

where $\psi = \beta/\alpha$ is the Fisher thermal rounding exponent, and α is an exponent that characterizes the shape of the energy landscape (see below).

Relatively little work has focused on the interplay between temperature effects and the scaling description for avalanches. Karmakar et al. also showed that, like with higher driving rates, increased temperatures interfere with avalanches, destroying their anomalous scaling with system size [32]. In that work, the stress-fluctuation scales can be worked out by determining the timescales of the system, and identifying when they compete with each other.

Subsequent to that work, there have been significant theoretical developments in the AQS regime, with scaling theories connecting different scale-free aspects of the

* djkorchi@phas.ubc.ca

yielding transition. One useful advance has been the notion of “residual stress” $x = \sigma_{th} - \sigma$, i.e. the stress necessary to trigger an ST with a threshold σ_{th} in a particular region of the amorphous solid. The distribution of residual stresses $p(x) \sim x^\theta$ is scale-free in the thermodynamic limit [12], and plays a key role in driving the anomalous stress-fluctuations in these systems. Mesoscale modelling has been particularly helpful in exploring scaling aspects of the yielding transition, as it coarse-grains at the level of STs, and directly exposes $p(x)$ [21].

To that end, in this work we will use a mesoscale model with Arrhenius activation rule (as in refs. [36–38])

$$\lambda(x) = \frac{1}{\tau} \exp\left(-\frac{x^\alpha}{T}\right), \quad (3)$$

to describe temperature and rate effects on the critical behaviour of the yielding transition. This choice of activation rule is motivated by an energy landscape picture: local regions of the amorphous solid are stable because there is an energy barrier (scaling as $U \sim Cx^\alpha$) preventing their rearrangement (with catastrophe theory suggesting $\alpha = 1.5$ [40]). Transition state theory suggests that temperature T causes repeated attempts at crossing these barriers, which succeed at a rate proportional to $\exp(-U(x)/k_B T)$ [41]. In this work, we set $C/k_B = 1$ and the prefactor τ^{-1} is set so that when $x = 0$ (i.e. no barrier), sites activate on average after τ , thus matching the microscopic timescale for ST rearrangement.

With the thermal timescale established, we begin by enumerating the other natural timescales in sheared amorphous solids:

- The plastic ST timescale τ over which atomistic rearrangements occur, i.e. the length of time for which a given ST is fluid and the timescale over which stress is dissipated.
- For a site a distance x from instability, the thermal Arrhenius activation timescale $1/\lambda(x) = \tau \exp(x^\alpha/T)$. In this description, sites with residual stress x have a potential barrier to thermal activation scaling as $U \sim x^\alpha$.
- For a site a distance x from instability, the mechanical yielding timescale $x/\mu\dot{\gamma}$, with μ a shear modulus.
- The average avalanche duration $\langle t \rangle_{av}$.
- The average loading time between triggering avalanches $\langle t_{load} \rangle$.

We will use the competition of these timescales to sketch out a phase diagram and predict the scaling in different regimes. Then, using numerical simulations, we will confirm the existence of the different phases and verify the scaling laws present in each phase.

II. THERMALLY ACTIVATED ELASTOPLASTIC MODEL

We use a mesoscale elastoplastic model (EPM), which coarse-grains the amorphous solid to a grid of L^d elastically coupled cells. Each cell i has a yield stress $\sigma_{th,i}$ drawn independently from a Weibull distribution (shape parameter $k = 2$) [42, 43] and an initial stress $\sigma_i = 0$. The system is driven at a fixed strain rate $\dot{\gamma}$ which adds stress uniformly to all sites at a global rate $\dot{x} = \mu\dot{\gamma}$. In the following we set $\mu = 1$. Sites fluidize immediately when their residual stress $x = \sigma_{th,i} - |\sigma_i| \leq 0$. Once fluid, sites remain fluid for 2τ , before again becoming elastic. Fluid sites dissipate stress as $\dot{\sigma}_i \sim -\sigma_i/\tau$. We use a finite-element solver to propagate stresses from fluidized sites, which automatically produces the anisotropic Eshelby-like stress-fields characteristic of STs. In contrast to the other thermally activated EPMs [36–38], we use a real-space stress-propagator more similar to [17, 44]. In some of our simulations, we follow refs. [16, 45] and shuffle the indices of the sites when applying the “kicks” from the fluidized sites and refer to these simulations as “shuffled-kernel” or mean-field (MF) simulations. There are two features that distinguish our model from the EPMs used in refs. [36–38]. Firstly, we study the system under constant strain-rate, as is more typical in MD simulations. This makes it challenging to numerically sample the time to failure for sites with $x \approx 1$, but can be accelerated for $\alpha = 1, 2$, to which we restrict our focus in this work. Secondly, our EPM implementation does not use periodic boundary conditions. For details on the acceleration algorithm and implementation details, see Appendix A.

III. COMPETITION OF TIMESCALES

Equation 3 implies a characteristic stress scale,

$$x_c = T^{1/\alpha}. \quad (4)$$

The Arrhenius activation rate is of order $1/\tau$ when $x \leq x_c(T)$. The first two natural timescales to equate are

$$x_c/\dot{x} = \tau, \quad (5)$$

which sets the mechanical yielding timescale for a site with residual stress x_c to the thermal yielding time for a site at or below x_c . This relation defines the orange line dividing regions 1 and 5 from 2, 3 and 4 in Fig. 1. For simulations with \dot{x} above this orange line, thermal effects are minimal, since even sites with $x < x_c$ are driven to mechanical failure at $x = 0$ before thermal activation can occur. For even higher shearing rates, when $\dot{x}\tau = 1$, sites injected at $x = 1$ yield within a single plastic timescale, creating a “mechanical fluid” in region 6.

The division between regions 2 and 3 comes from competition between finite-size scaling and the thermal activation of sites. In steady state, the average stress dissipated by avalanches (whose size S is defined by the stress

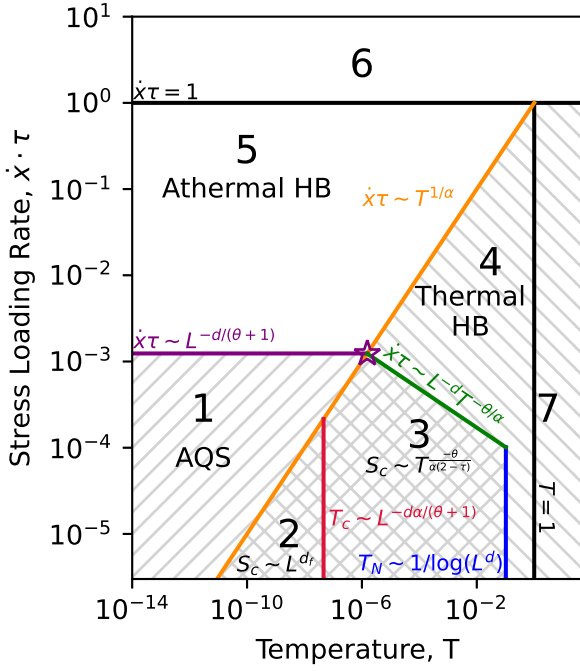


FIG. 1. Dynamical phase diagram for the thermal two-dimensional EPM at $L = 128$ for $\alpha = 2$. Blue, green, red, and purple lines have finite-size scaling with L . “//” hatching indicates a region with non-overlapping avalanches. “\” hatching indicates thermal effects are prevalent.

drop during the avalanche as $S = L^d \delta \Sigma_{av}$) must equal the stress loaded between avalanches: $\langle t_{load} \rangle \dot{x} = L^{-d} \langle S \rangle = \langle \delta \Sigma \rangle_{av}$. Since $\langle t_{load} \rangle(L)$ scales with L , this produces a non-trivial scaling for the mean avalanche size $\langle S \rangle$. In the athermal case, an avalanche begins when the weakest site (left at x_{min} by the preceding avalanche) reaches $x = 0$, so in AQS $\langle t_{load} \rangle \dot{x} = \langle x_{min} \rangle$. If x is independent between sites (which appears to be approximately true), $\langle x_{min} \rangle$ is set entirely by $p(x)$, with $L^{-d} = \int_0^{\langle x_{min} \rangle} p(x') dx'$. However, thermal effects alter the form of $p(x)$ from the power-law form $p(x) \sim x^\theta$ expected in the thermodynamic limit.

As can be seen in Appendix B (Fig. 10), so long as $\dot{x} < x_c/\tau$ (i.e. in the thermal regime) sites below x_c are rare. If we approximate $p(x) = Ax^\theta$ for $x \in (x_c, 1)$ and elsewhere zero and use $L^{-d} = \int_0^{\langle x_{min} \rangle} p(x') dx'$, we obtain:

$$\langle x_{min} \rangle = \left(\frac{\theta + 1}{A} L^{-d} + x_c^{\theta+1} \right)^{1/(\theta+1)}, \quad (6)$$

which is valid whenever thermal activations occur quickly compared to mechanical yielding (i.e. in regions 2, 3, and 4). Clearly, there is a natural temperature scale when $x_c^{\theta+1} \sim L^{-d}$, i.e. when

$$T_c \sim L^{-d\alpha/(\theta+1)}. \quad (7)$$

This is the red line dividing regions 2 & 3. The transition across this line is detailed in section IV A.

At high driving rates, amorphous solids exhibit a characteristic shear-thinning stress response, typically captured by the Herschel-Bulkley relation (eq. 1): $\dot{\gamma}^n \sim \Sigma - \Sigma_c$, where $n = 1/\beta$ is the Herschel-Bulkley exponent. A typical 2d value for the Herschel-Bulkley exponent found in EPMS is $n \approx 2/3$ [12]. In experiments, $n \in [0.4, 1]$ have been reported, and indeed n can vary systematically in response to temperature [34] and pH [46]. The rise in stress with strain rate occurs because avalanches begin to overlap, i.e. the loading time is comparable to the duration of avalanches [32]. The next several relations determine the onset of avalanche overlap. An avalanche continues indefinitely, as long as the time between shear-transformation zone activations is less than τ . Hence, we can establish a maximum shear rate of $\tau \dot{x} = 1$, which divides regions 5 and 6. Similarly, we can establish a maximum temperature, T_N , for which avalanches in a finite-size system remain discrete by setting the rate of activation for L^d freshly injected sites equal to $1/\tau$:

$$\tau^{-1} = \frac{L^d}{\tau} e^{-1^\alpha/T_N} \quad (8)$$

implying $T_N = 1/\log(L^d)$. This is the blue line dividing regions 3 and 4. At an even greater temperature, $T = 1$, freshly injected sites at $x = 1$ will yield within one plastic timescale τ , setting the threshold for the “thermal fluid” in region 7. In this region, the stress accumulated during time τ is $\Sigma = \tau \cdot \dot{x}$ and so the system is well described by a simple Newtonian fluid (i.e. $\Sigma_c = 0$ and $n = 1$). Since mechanical fluidization can initiate even faster than the Arrhenius rate, region 6 dominates over region 7.

For non-molten temperatures and lower-rates, avalanches can overlap because the loading time between avalanches is comparable to the plastic time i.e.:

$$\langle t_{load} \rangle = \tau. \quad (9)$$

We first handle the thermally assisted case (i.e. $\dot{x} \tau < T^{1/\alpha}$). When thermal activation occurs at x_c , $\langle t_{load} \rangle = (\langle x_{min} \rangle - x_c)/\dot{x}$. For $T > T_c(L)$, we can expand eq. 6 to first order in L^{-d} giving:

$$\langle t_{load} \rangle = \frac{1}{\dot{x}} [x_c^{-\theta} L^{-d}]. \quad (10)$$

Using $\langle t_{load} \rangle = \tau$ and $x_c = T^{1/\alpha}$ we find:

$$\dot{x} \tau \sim L^{-d} T^{-\theta/\alpha}. \quad (11)$$

This gives the green line dividing region 3 and 4 in Fig. 1. Now for the second case, where $T < (T_c)^\alpha$, we know that thermal activation should be rare (i.e. mechanical effects dominate). Then, the form of $p(x)$ is altered to have a size and drift velocity dependent plateau for $x < x_p \sim (\tau \dot{x} + 0.02L^{-2})$ (see Appendix B Fig. 10). If we instead use that $\langle x_{min} \rangle$ is in the plateau (an appropriate assumption for large L), we have

$$\langle x_{min} \rangle = L^{-d} p_0^{-1} \quad (12)$$

where $p_0 = Ax_p^\theta$. Then, equating the loading time and the ST plastic time, we have:

$$\tau = \langle x_{\min} \rangle / \dot{x} = \frac{L^{-d}}{\dot{x}(\tau\dot{x} + 0.02L^{-2})^\theta} \quad (13)$$

which yields the purple line, dividing region 1 and 5. For large L , this simply becomes

$$\dot{x} \sim L^{-d/(1+\theta)}. \quad (14)$$

We have found phase lines (eqs. 11,14) for avalanche overlap on both sides of the thermal activation phase line $\dot{x}\tau \sim T^{1/\alpha}$. These phase lines should be continuous across the thermal activation phase line, which implies a system size dependent temperature $T_{overlap}$:

$$L^{-d/(1+\theta)} \sim L^{-d}T_{overlap}^{-\theta/\alpha} \implies T_{overlap} \sim L^{\frac{-d\alpha}{1+\theta}}, \quad (15)$$

which we indicate with the purple star in the phase diagram. We note that $T_{overlap}$ has the same finite-size scaling as the temperature scale for which temperature truncates avalanche sizes (eq. 7). Transitions across these lines are explored in section IV B.

IV. NUMERICAL TESTS OF THE PHASE DIAGRAM

To test our phase diagram and scaling theory, we perform simulations at different stress-loading rates \dot{x} , temperatures T , system sizes L , and with $\alpha = 1$ and $\alpha = 2$, as well as for 2d simulations and 2d simulations with a shuffled kernel. These shuffled kernel simulations keep the broad-tailed kick statistics of the 2d simulations, but remove spatial correlations between sites, thus providing a mean-field (MF) realization of the EPM [16]. One consequence of this is that the exponent θ changes from $\theta \approx 0.52$ (in 2d) to $\theta \approx 0.35$, allowing us to vary θ and test scaling relations involving θ . For convenience of the reader, Fig. 2 presents an overview of the regions of the phase-diagram that were simulated, and indicates the corresponding figures.

A. Avalanche size cutoff

Discrete avalanches exist in regions 1, 2, and 3. In region 1, avalanches do not overlap and thermal activations do not occur, making this the well-studied AQS limit.

In zone 3, where thermal effects are large, we expect: $\langle t_{load} \rangle \sim L^{-d}T^{-\theta/\alpha}$ (eq. 10), so that

$$\langle S \rangle \sim T^{-\theta/\alpha} \quad (16)$$

(i.e. no system-size dependence of the mean avalanche size). Meanwhile, for $T \ll T_c$ (i.e. $x_c^{1+\theta} \ll L^{-d}$), eq. 6 reduces to simply $\langle x_{\min} \rangle \sim L^{-d/(\theta+1)}$. For $\dot{x}\langle t_{load} \rangle = \langle x_{\min} \rangle - x_c$ with $x_c \ll L^{-d/(1+\theta)}$, we simply

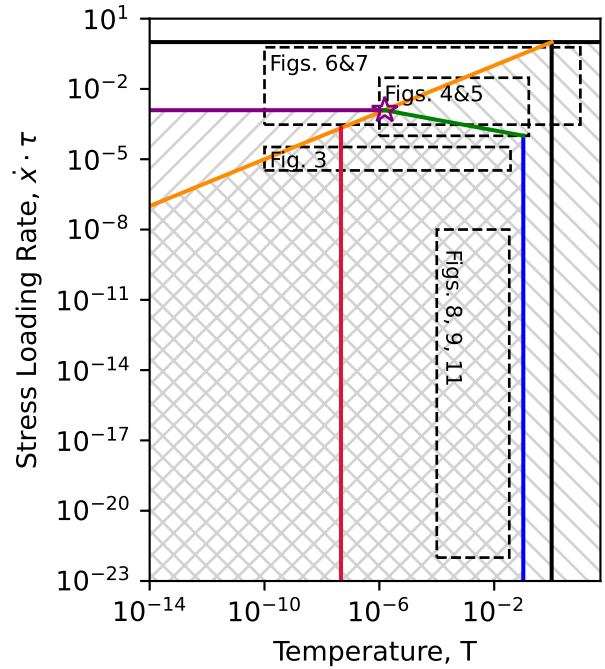


FIG. 2. The phase diagram, as in Fig. 1, but the regions of phase space explored in different figures marked by rectangles.

have $\langle \delta\Sigma \rangle_{av} = \dot{x}\langle t_{load} \rangle = \langle x_{\min} \rangle$. Hence, in the low-temperature limit, $\langle S \rangle_{AQS} \sim L^{d\theta/(\theta+1)}$.

In Fig. 3, we verify this scaling for $\langle S \rangle$ crossing the 1-2 phase line, using $x = (T/T_c)^{\theta/\alpha}$ and $y = \langle S \rangle / \langle S \rangle_{AQS}$, which collapses the AQS plateau and gives a high-temperature tail scaling as x^{-1} . We find almost no driving-rate dependence in the avalanche size, except for those simulations close to T_N (orange in Fig. 3), where lower velocities weakly decrease avalanche size due to stress-softening. For this reason, the highest temperature fall slightly below the $T^{-\theta/\alpha}$ scaling. Now, assuming a power-law form for the distribution of avalanche sizes $p(S) \sim S^{-\tau}g(S/S_c(T, L))$, truncated at S_c , we have that:

$$\langle S \rangle = \int_0^\infty s^{1-\tau}g(s/s_c)ds = s_c^{2-\tau} \int_0^\infty u^{1-\tau}g(u)du, \quad (17)$$

implying

$$\langle S \rangle \sim s_c^{2-\tau}. \quad (18)$$

Coupled with $\langle S \rangle \sim T^{-\theta/\alpha}$ this implies $s_c(T) \sim T^{-\theta/(\alpha(2-\tau))}$. Meanwhile, for $T < T_c(L)$, we have the usual AQS regime scaling, $s_c(L) \sim L^{d/((\theta+1)(2-\tau))}$ and consequently the scaling relation $d_f = d/((\theta+1)(2-\tau))$ [21]. Though this works well for the shuffled kernel simulations, we note that for our full 2d simulations, there are small corrections due to finite-size scaling effects in $p(x)$ as described previously [47].

Our finding, that there are “anomalous” stress fluctuations (i.e. $\langle \Delta\Sigma \rangle_{av} \lesssim N^{-1}$) below a critical temperature related to the size of the system, and “normal” (i.e.

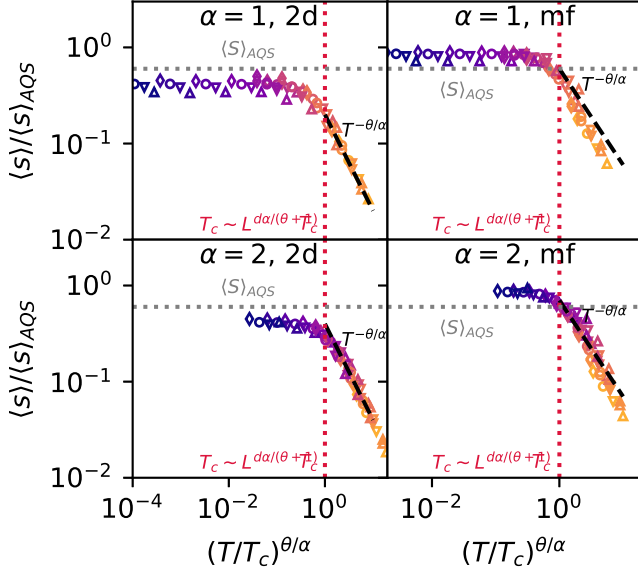


FIG. 3. Rescaled mean avalanche sizes for $\dot{x}\tau = 10^{-5}$. Lighter colours are hotter temperatures $T \in (10^{-10}, 0.037)$, symbols indicate system sizes ranging from $L = 32$ to $L = 256$. $\langle S \rangle_{AQS}$ scales as $\langle S \rangle_{AQS} \sim L^{d\theta/(\theta+1)}$ and $T_c \sim L^{d\alpha/(\theta+1)}$, these scalings are indicated with the dotted lines.

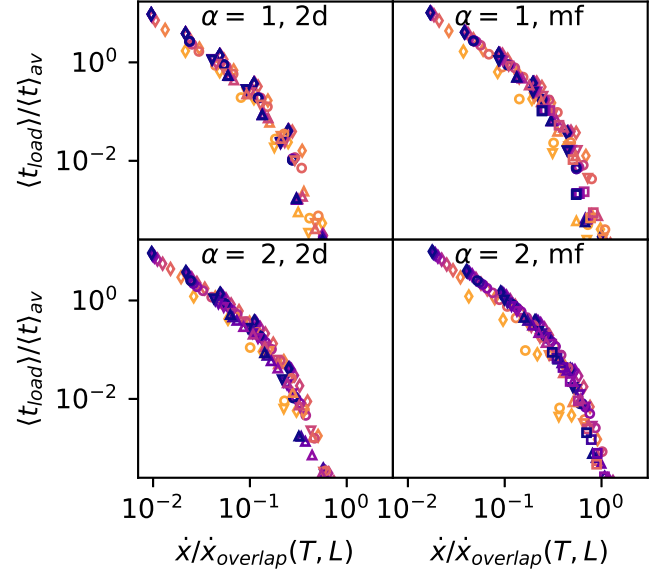


FIG. 5. Finite-size scaling collapse for the avalanche overlap parameter, for simulations with different temperatures (lighter colors show higher temperatures) and system sizes (differing symbols).

B. Avalanche overlap onset

Herschel-Bulkley power-law scaling occurs because the timescale of avalanches is comparable to the timescale between loading, and so stress is added to the system faster than avalanches can release it. It is therefore natural to consider the ratio of time-scales: $\langle t_{load} \rangle / \langle t_{av} \rangle$. As avalanches overlap more and more, the durations between avalanches should become exponentially shorter and rarer, as can be seen in Fig. 4. It is clear that there is a temperature dependence in these curves, but also that for many temperatures the results are identical. This is consistent with our phase diagram in Fig. 1, where avalanche overlap occurs at fixed $\dot{x} \sim L^{-d/(1+\theta)}$ for $\dot{x} > \dot{x}_c(T)$ and at $\dot{x} \sim L^{-d}T^{-\theta/\alpha}$ for $\dot{x} < \dot{x}_c(T)$. We can capture both scaling behaviours with the phenomenological scaling function

$$\tau \dot{x}_{overlap}(T) \sim L^{-d/(\theta+1)} (1 + (T/T_{overlap})^{s\theta/\alpha})^{-1/s} \quad (19)$$

which is characterized by a phenomenological sharpness parameter s (which we here take to be 2), and for the overlap temperature $T_{overlap} = CL^{-d\alpha/(1+\theta)}$, where C is an arbitrary constant prefactor (eq. 15). We find that $C \approx 2$ for $\alpha = 1$ and $C \approx 20$ for $\alpha = 2$ produces an effective collapse for simulations with varying temperature and system size in Fig. 5.

C. Rheology transition across $\dot{x}_c(T)$

For strain rates above the avalanche-overlap threshold, the Herschel-Bulkley law $\dot{\gamma} \sim ((\Sigma) - \Sigma_c(T))^n$ is a

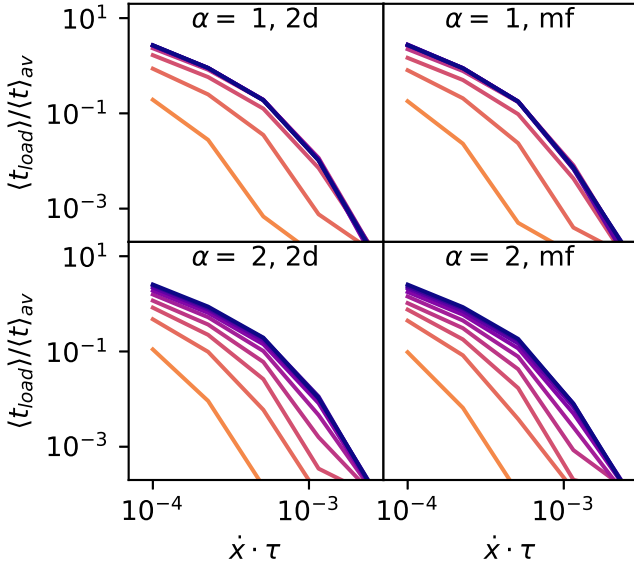


FIG. 4. Degree of avalanche overlap, as measured by the ratio of the waiting time and the average avalanche duration, for $L = 64$. Lighter colors are hotter temperatures.

$\langle \Delta \Sigma \rangle_{av} \sim N^{-1}$) fluctuations above this temperature, reflects the results previously identified by Karmakar et al. with particle scale simulations [32, 48].

reasonable fit to our data (cf. Fig. 6). We observe that at high strain-rates (above $\tau \dot{x}_c \sim T^{1/\alpha}$), stress becomes independent of temperature. However simulations above a certain temperature show a decrease in the fitted flow stress and in the rheological exponent n . At still higher temperatures ($T > 1$) the rheological exponent tends to $n = 1$ as would be expected for a simple fluid.

That the rheological exponent changes with n should not surprise experimentalists, where temperature-dependent viscosity effects have been seen to alter the rheological exponent [34]. However, since the exponent $1/n = \beta$ has been proposed to scale as $\beta = 1 + z/(d - d_f)$ [49], naively this would suggest that the avalanche critical exponents would continuously vary with temperature. However, as we show below, this effect can be simply understood as fitting through two exponents operating in different regimes.

To expose this effect, in Fig. 7 we consider the stress-rise above the flow stress $\Sigma_c(T)$ and divide out the AQS Herschel-Bulkley exponent n_{aqs} . Although the decrease in n appears gradual in Fig. 6, our data in Fig. 7 shows that the transition is actually sharp: there is a thermal and an athermal n exponent. Temperature effects seem to approximately halve the observed Herschel-Bulkley exponent n . By studying the stress-rise above $\Sigma_c(T)$, we find that the athermal value n_{aqs} dominates when $\dot{x} > \dot{x}_c \sim T^{1/\alpha}/\tau$ (cf. Fig. 7). The apparent intermediate values of n in Fig. 6 are a result of fitting through both regimes. At very high T , the stress scales simply as $\langle \Sigma \rangle \sim \tau \cdot \dot{x}$, i.e. $n = 1$.

V. THERMALLY TRUNCATED AVALANCHES

We have provided numerical evidence for the existence of different dynamic phases in our phase diagram. Now we seek to clarify the effect of temperature on the well-defined avalanches in region 3 of the phase diagram. There, temperature is high enough to overcome finite-size effects, while remaining low enough that (with sufficiently slow driving) avalanches do not overlap. In this case, as we showed previously, the average avalanche size scales as $\langle S \rangle \sim T^{-\theta/\alpha}$, and owing to eq. 18, we have that $s_c \sim T^{-\theta/(\alpha(2-\tau))}$.

However, if driving rates are lowered far below the Herschel-Bulkley onset, a thermal softening of the material occurs as even nominally stable sites above $x_c = T^{1/\alpha}$ can be activated and the mean flow stress $\langle \Sigma \rangle$ is depressed by temperature (see Fig. 6). At extremely low strain-rates (in our data, with $\dot{x}\tau \in (10^{-22}, 10^{-9})$), there is additional softening below the apparent plateau present in Fig. 6. This softening introduces a stress gap, $\langle \Delta \Sigma \rangle(T, \dot{x}) = \langle \Sigma \rangle_{aqs} - \langle \Sigma \rangle(T, \dot{x})$, which means that, on average, there is less energy available for avalanches to propagate.

The stress gap introduces a power-law scaling in avalanche size cutoff, $s_c \sim |\Delta \Sigma|^{-1/\sigma}$, with a new exponent $1/\sigma$. This exponent has been measured in EPM

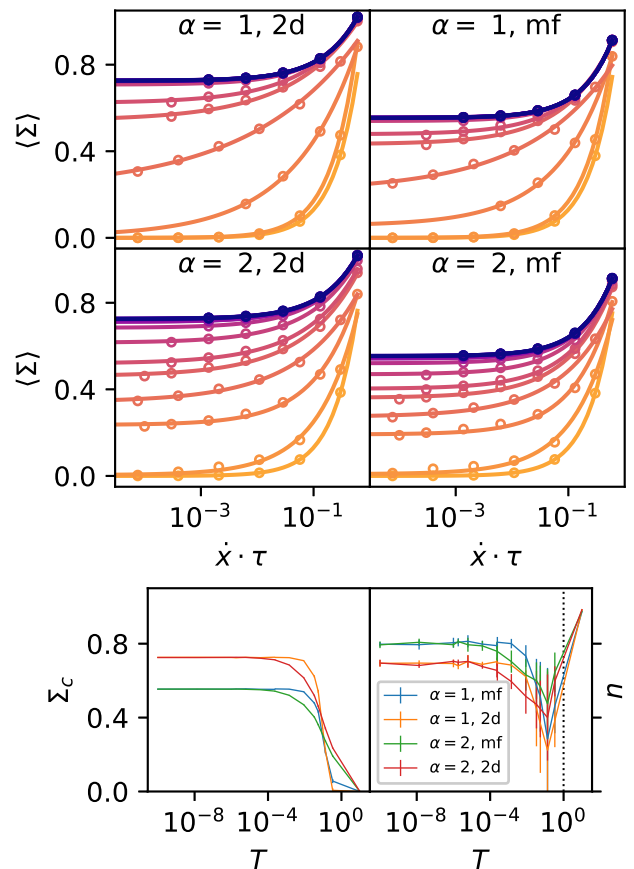


FIG. 6. Rheology data with Herschel-Bulkley fits for fixed system size $L = 64$, allowing both exponent n and the temperature dependent stress-plateau $\Sigma_c(T)$ to vary. T varies from 10^{-10} to $3 \cdot 10^{-1}$. Bottom: fitted Σ_c and n values vary with temperature.

by fixing the stress of the system with $\Sigma < \Sigma_c$ and artificially triggering an avalanche by kicking a random site [17] or by measuring avalanches in the approach to steady-state flow [50]. However with the temperature dependent stress-gap entering, $1/\sigma$ can be probed naturally, by considering the mean-avalanche size for simulations at slow driving, where eq. 18 implies

$$\langle S \rangle \sim |\Delta \Sigma|^{(\tau-2)/\sigma}. \quad (20)$$

Our data in Fig. 8 is consistent with $\sigma \approx 1.1$. To the best of our knowledge, this is the first time this exponent has been measured in a strain-controlled simulation. This value of σ is higher than previous reports. In ref. [17], where stress was fixed below the flow stress and random sites were kicked, $\sigma \approx 0.51$, while in ref. [50], where avalanches were measured as the system were loaded to its critical point, $1/\sigma \approx 0.59$ (inferred from the scaling relation eq. 20). Our explanation for this discrepancy is the following: avalanche propagation depends on the number of sites with small residual stress and on correlations between sites. We propose that $1/\sigma$ therefore depends on how the stress gap $\Delta \Sigma$ is established. In our case, sites

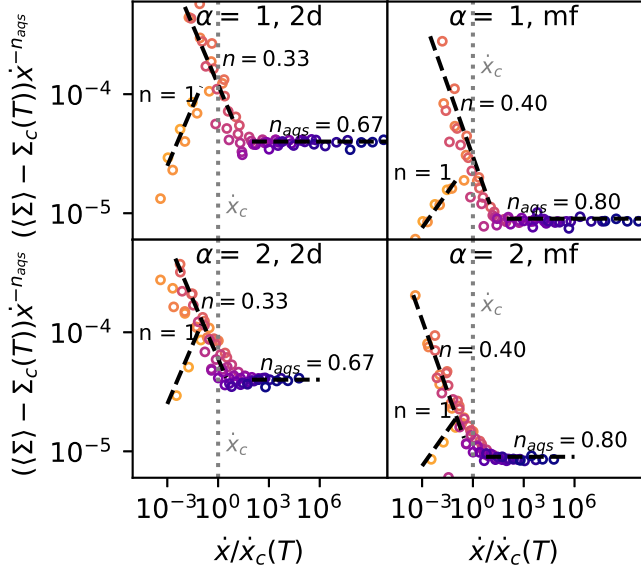


FIG. 7. Rheology data, rescaled to exhibit a change in Herschel-Bulkley exponent n for $\dot{x} > \dot{x}_c(T) \sim \frac{1}{\tau} T^{1/\alpha}$. The AQS limit for n_{ags} is included in the rescaling to make the transition to the thermal value n_{th} more evident. Simulations at $T = 10$ in the molten phase (brightest orange) obey $n = 1$ scaling.

with $x < x_c(T)$ (and for low driving, sites $x \approx x_c$) are suppressed. In the above mentioned works, the $p(x)$ distribution evolved with the stress gap, with substantially lower values of θ reported.

In any case, if we combine eq. 16 and eq. 20, we obtain

$$\Sigma_c(T = 0, \dot{\gamma} \ll 1) - \Sigma(T, \dot{\gamma}) = \Delta\Sigma \sim T^{\theta\sigma/(\alpha(2-\tau))}, \quad (21)$$

which collapses our low strain-rate stress-gap data (cf. fig. 9). This scaling argument doesn't account for strain-rate effects, but we find that these are relatively modest.

In prior work on the problem of thermally activated flow in amorphous solids, the characteristic stress scale was identified as $\Delta\Sigma \sim T^{1/\alpha}$, per eq. 2 and the strain-rate is scaled by the thermal yielding exponent $\psi = \beta/\alpha$ as $\dot{\gamma}/T^{\beta/\alpha}$ [36, 37]. We find that this scaling does not effectively collapse our low strain-rate simulations (see the dashed lines in Fig. 9). We do find this $T^{1/\alpha}$ scaling for simulations in the flowing state (i.e. with overlapping avalanches) in Fig. 7. Meanwhile, in the jerky steady-state with non-overlapping avalanches, we find a small correction to this scaling, with $\Delta\Sigma \sim T^{0.8/\alpha}$. Why do different stress-scales appear between jerky flow and rheological flow? In the case of non-overlapping avalanches, the appropriate stress-scale is set by the typical stress dissipated by a single avalanche $\langle S \rangle \sim |\Delta\Sigma|^{(\tau-2)/\sigma}$. Once avalanches overlap the pertinent stress scale in the problem changes to reflect the stress scale of yielding sites, $x_c \sim T^{1/\alpha}$.

This correction at low strain-rates may not have been previously noted because the difference in scaling between $T^{1/\alpha}$ and $T^{0.8/\alpha}$ (see Fig. 9) is relatively small.

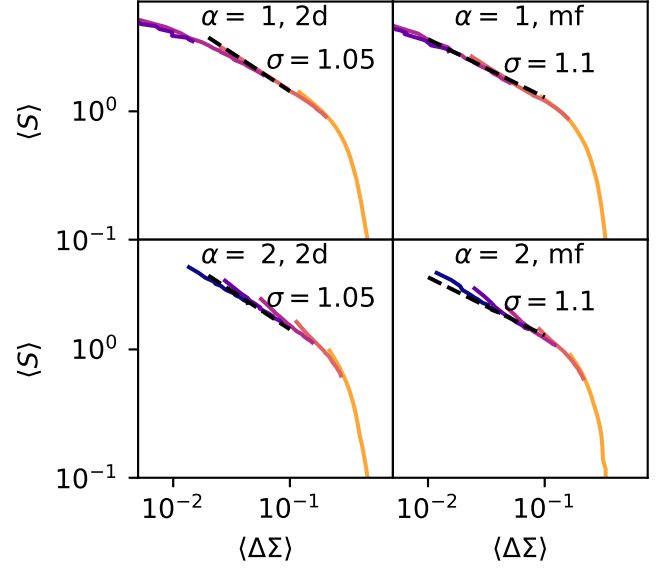


FIG. 8. Power-law scaling for mean avalanche size with the stress-gap created at extremely slow driving. Power-law fit uses $\tau = 3/2$ for mean-field (mf) data and $\tau \approx 1.37$ for 2d data. Dashed lines scaling are set by eq. 20, with indicated fit values of σ .

The difference is only obvious when excluding the data from the Herschel Bulkley regime (where the $T^{1/\alpha}$ scaling is correct) — if the data from the Herschel Bulkley regime is included, this gap is visually compressed. It is also possible that this alteration in scaling is because we use strain-controlled simulations, while previous efforts on this problem used stress-controlled simulations.

VI. CONCLUSIONS

We have derived a schematic dynamic phase diagram for sheared amorphous at finite temperature by comparing the main timescales of the problem. Using EPM simulations, we have provided numerical evidence for these phase lines, by varying the exponent α , and by use of a shuffled-kernel, the exponent θ . The main phase lines dictate whether thermal activation occurs and whether avalanches overlap. Avalanche overlap has strong finite-size effects, while the threshold for thermal effects is size independent. In the infinite system size limit, the strict AQS critical point occurs only for $T = 0$ and $\dot{x} = 0$. Avalanches can be truncated by either finite-size effects or by temperature, and we have derived appropriate scaling arguments for both cases.

These simulations complement prior stress-controlled work, and agree with $\Delta\Sigma \sim T^{1/\alpha}$ as the appropriate stress scale when avalanches overlap [36, 37]. When avalanches do not overlap, i.e. before Herschel-Bulkley flow onset in the low-strain rate limit, thermal effects soften the material and introduce a new temperature-dependent stress gap. Using scaling arguments, we

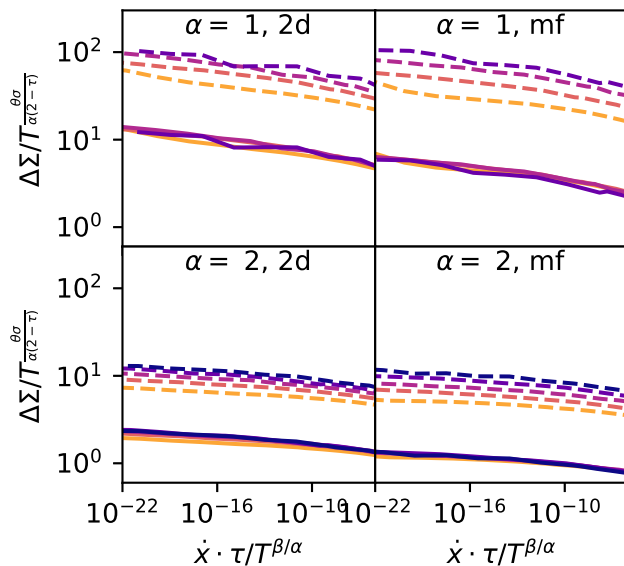


FIG. 9. The stress-softening effect, collapsed according to our proposed scaling $\Delta\Sigma \sim T^{\frac{\theta\sigma}{\alpha(2-\tau)}}$ (solid lines) and according to the previously proposed scaling $\Delta\Sigma \sim T^{1/\alpha}$ (dashed lines) for both for the shuffled kernel and 2d simulations. For clarity, the dashed lines have been shifted vertically by a factor of 3. All simulations are $L = 64$, and $T \in (10^{-4}, 3 \cdot 10^{-2})$, see Table. I for exponent used in collapse.

have linked that stress gap to the stress dissipated by avalanches, finding $\Delta\Sigma \sim T^{(\theta\sigma)/(\alpha(2-\tau))}$. Intriguingly, this brings the AQS $1/\sigma$ exponent, which is normally only exposed by stress-controlled simulations, into the thermal problem. Since we arrived at that scaling using generic scaling arguments, it should also hold in stress-controlled simulations.

One avenue that this work does not touch on is aging and thermal history dependence. We use a fixed Weibull distribution for site yield thresholds σ_{th} , but this distribution has been shown to have temperature dependence [51, 52]. To what extent this affects critical behaviour beyond the ductile-brittle transition has not been elucidated.

One aspect that deserves further study is why the thermal Herschel-Bulkley exponent takes the value it does. Can this be linked by appropriate scaling arguments to the other critical exponents, as is done in the athermal case [12, 49]? An accurate space-time exponent z would need to be measured, along with the correlation length exponent ν (or its thermal equivalent). One intriguing aspect is our observation that both the thermal and athermal Herschel-Bulkley exponent differ when the kernel is shuffled and correlations between sites are destroyed. This seems to suggest that not all aspects of the yielding transition are mean-field.

ACKNOWLEDGMENTS

This research was undertaken thanks, in part, to funding from the Canada First Research Excellence Fund, Quantum Materials and Future Technologies Program. DK thanks NSERC for financial support through a CGS-D scholarship.

Appendix A: Implementation Details

1. Loading times

Sites liquefy by thermal activations at rate $\lambda(x)$, or immediately at $x = 0$. To simulate the dynamics of our systems, we essentially need to work out which site i will fail next and at what time δt (while correctly accounting for loaded stress \dot{x}). Once the next site to liquefy is known, stress relaxation at the site and stresses propagated from that site can be worked out using the finite element solver. All sites have their stresses increased by $\dot{x} \cdot \delta t$ and any propagated stresses or relaxations $\sim \exp[-\delta t/\tau]$ applied.

Working out the inter-event period δt and site i is relatively trivial for fixed stress simulations between avalanches, where activations happen at fixed rate $\lambda(x)$. Since activations are independent Poisson processes, with an exponentially decaying waiting time $\rho(t) = \lambda(x_i)e^{-\lambda(x_i)t}$, for a system with $N = L^d$ sites one could sample N random numbers $\{U_i \in [0, 1]\}$, and find the next activation time for each site by inverting the cumulative distribution function for the exponentially distributed waiting times, so that each site is assigned a time: $t_i = \frac{-1}{\lambda(x_i)} \log(1 - U_i)$. By finding the i with the smallest t_i , one has found the first site the yield, and the appropriate interval $\delta t = t_i$. This naive scheme could obviously be improved by using a global rate, $\lambda = \sum_i \lambda(x_i)$ and choosing a site i at random with weight $\lambda(x_i)$, which reduces the problem to requiring only two random numbers, instead of N .

In our system, because σ_i evolves in time as

$$\sigma_i(t) = \sigma_{i,0} + \dot{x}t + \sigma_i^{applied}(1 - e^{-t/\tau}) \quad (\text{A1})$$

where $\sigma_i^{applied}$ are the stresses propagating from liquefied sites to site i , the Poisson rates $\lambda(x_i)$ are not constant. We follow the “naive” approach, but generalized to inhomogeneous Poisson processes, for each site sampling a random number $U_i \in [0, 1]$, and solving for t_i as:

$$U_i = P(t < t_i) = \exp\left[-\int_0^{t_i} \lambda(x_i(t))dt\right]. \quad (\text{A2})$$

As before, once we have a t_i for each site, we pick the lowest t_i for δt and liquefy site i . In practice, we solve eq. A2 in two ways: (i) after all $\sigma_i^{applied}$ have decayed by 25τ and are negligible, $\sigma_i(t)$ are linear in time, and eq. A2 can be solved and inverted analytically for $\alpha = 1$

and $\alpha = 2$ (ii) when $\sigma_i(t)$ are non-linear, we solve eq. A2 numerically by constructing and solving a related initial value problem (IVP).

For the analytical case, using $\lambda(x) = \frac{1}{\tau} \exp(-x^\alpha/T)$ we restrict ourselves to $\alpha = 1$ and $\alpha = 2$. For $\alpha = 1$, with $x(t) = \sigma_{th} - (\sigma_0 - \dot{x}t)$ (suppressing the i subscripts for brevity), we have

$$\int_0^{t_i} \lambda(x(t)) dt = \frac{T}{\dot{x}\tau} e^{-(\sigma_{th}-\sigma_0)/T} \left(e^{t_i \dot{x}/T} - 1 \right).$$

Since $U_i = 1 - e^{\int_0^{t_i} \lambda(x_i(t)) dt}$, we can solve for t_i as:

$$t_i = \frac{\sigma_{th} - \sigma_0}{\dot{x}} + \frac{T}{\dot{x}} \log \left[e^{-(\sigma_{th}-\sigma_0)/T} + \log(1 - U_i) \frac{\tau \dot{x}}{T} \right],$$

where we can recognize the first term as the mechanical yielding timescale $(\sigma_{th} - \sigma_0)/\dot{x} = x/\mu\dot{\gamma}$, and the second as a temperature-dependent stochastic correction that can reduce the time to yield. The $\alpha = 2$ case is similar, and gives:

$$t_i = + \frac{\sigma_{th} - \sigma_0}{\dot{x}} - \frac{\sqrt{T}}{\dot{x}} \operatorname{erf}^{-1} \left[\operatorname{erf} \left(\frac{\sigma_{th} - \sigma_0}{\sqrt{T}} \right) + \frac{2\dot{x}\tau}{\sqrt{\pi T}} \log(1 - U_i) \right].$$

These analytical equations are used between avalanches for potentially very long loading periods. This avoids a potentially expensive numerical integration at each site, since a small time-step (comparable to τ) is necessary to avoid missing the thermal activation of a site (since a site approaching $x \approx x_c = T^{1/\alpha}$ activates on average on a timescale $\approx \tau$). In practice, since $x \equiv \sigma_{th} - |\sigma|$, we also consider the case $x(t) = \sigma_{th} + \sigma_0 - \dot{x}t$ to catch the (rare) events in which negatively stressed sites yield thermally. Additionally, these equations are prone to numerical under/overflows, so care must be taken when implementing these equations to deal with potential numerical pitfalls.

The numerical description is conceptually simpler, though more computationally expensive. To solve eq. A2 numerically, consider the obviously related function $U(t) = \exp \left[- \int_0^t \lambda(x_i(t')) dt' \right]$, for which $U(t_i) = U_i$ is our desired solution. $U(t)$ obeys the following differential equation:

$$\frac{dU}{dt} = (1 - U(t)) \lambda(x_i(t)), \quad (\text{A3})$$

for which the IVP $U(t=0) = 0$ and $U(t_i) = U_i$ (where U_i is still randomly drawn from $[0, 1)$) has a unique solution. We use SciPy's `solve_ivp` routine [53] to integrate these equations for all sites simultaneously – halting when either $U(t_i) = U_i$ for a site or $x_i = 0$ for a site. As in the analytical case, we consider both cases of $x_i = \sigma_{th} \pm \sigma_i(t)$, allowing for a site to yield because it is stressed too far in either direction. Since the Eshelby-like stress-propagator has both positive and negative kicks, sites frequently fail in either direction during an avalanche (though they are biased to fail in the forward loading direction).

2. Stress Propagator and Shuffled Kernel

When sites liquefy, they reduce their stress and re-distribute stresses elsewhere in the system. We use the finite-element method on a regular triangular mesh to determine the stress propagation between sites. Each square site in the system consists of four finite-element triangles terminating in a central vertex. We use first-order Lagrange elements for the displacement field \underline{u} , and zeroth-order discontinuous Galerkin elements to represent the stresses, strains, and plastic strains on the plaquettes. We relate the total strain to the displacement as,

$$\underline{\underline{\gamma}} = \frac{1}{2} [(\nabla \underline{u}) + (\nabla \underline{u})^T] \quad (\text{A4})$$

and decompose the strain tensor into plastic (stress-free) and elastic parts as: $\underline{\underline{\gamma}} = \underline{\underline{\gamma}}_{pl} + \underline{\underline{\gamma}}_{el}$. The elastic-strain contributes to the tensorial stress as:

$$\underline{\underline{\sigma}} = 2\mu \underline{\underline{\gamma}}_{el} + \lambda \operatorname{tr}(\underline{\underline{\gamma}}_{el}) \mathbb{1}, \quad (\text{A5})$$

where, for our simulations, we use $\mu = 1$ and $\lambda = \frac{1}{2}$. The local stress σ_i at a site i is the average $\underline{\underline{\sigma}}_{xy}$ component of the stress over the square cell. To work out the long-time stress-field from a liquefied site, we increment the plastic strain at that site (equally distributed over all triangles) by the stress at the site. We then solve the elastic equations, and find the stress-increments $\delta\sigma_{ij}$ at all sites in the system. For each site j in the system, we then set $\sigma_j^{applied} \rightarrow \sigma_j^{applied} + \delta\sigma_{ij}$, so that this stress-increment is applied exponentially over the next several time units τ .

For the shuffled-kernel simulations, we first identify a central site i in the system (e.g. for $L = 32$ at $(x, y) = (15, 15)$). We then apply a nominal plastic strain of magnitude 1, and work out the resulting $\delta\sigma_{ij}$ at all sites. The resulting set of $N - 1$ stress-increments are $\{\delta\sigma_{ij}\}$ then stored for later use, so that the expensive finite-element calculation is not repeated throughout the mean-field simulations. When a site k in the shuffled-kernel simulation fails, all sites receive a stress-increment $\sigma_j^{applied} \rightarrow \sigma_j^{applied} + \sigma_k \delta\sigma_{ij'}$, where the j' are drawn without replacement from $\{1, 2, \dots, i - 1, i + 1, \dots, N\}$. The failing site of course receives the stress-increment $\sigma_k^{applied} = \sigma_k \delta\sigma_{ii} \approx -\sigma_k$. In this way, the stress increments initially calculated for a central site are shuffled for the non-failing site, and scaled according to the stress at the failing site, and the failing site relaxes in accordance to its stress.

Appendix B: $p(x)$ form

For simulations with well-defined avalanches, $p(x)$ can be sampled immediately after each avalanche. The distribution of $p(x)$ then can be used to predict the loading

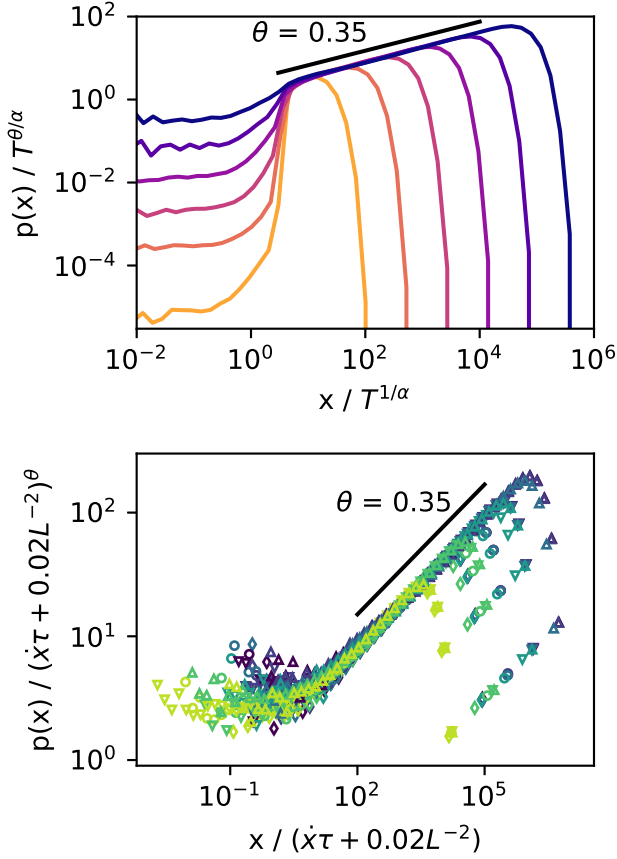


FIG. 10. The residual stress distributions of shuffled kernel simulations ($\theta = 0.35$), rescaled by characteristic scales set by temperature, velocity, or finite-size effects. Top: $p(x)$ for simulations with different values of T (brighter colours have higher T) and $L = 256$, rescaled by $x_c = T^{1/\alpha}$ for low velocities. Bottom: $p(x)$ for simulations with different values of v (brighter colours have higher strain rate) and L (indicated by symbol), rescaled by $x_p = (\tau\dot{\gamma} + 0.02L^{-2})$.

time before the next avalanche. For simulations in with $\dot{x} < \dot{x}_c(T)$, we find that $P(x)$ takes the form of a power-law with an exponential cut-off at $x < x_c = T^{1/\alpha}$, as can be seen in Fig. 10. For simulations with a higher-driving rate however, there is a system-size dependent and velocity dependent plateau (Fig. 10). We expect the velocity dependent plateau to occur at $x \approx \tau \cdot \dot{x}$, while the system-size dependent terminal plateau should scale as $x \sim L^{-d}$ [44, 47]. We approximate the plateau as occurring at $x_p = (\tau\dot{\gamma} + 0.02L^{-2})$, which effectively collapses the plateau onset in Fig. 10.

Appendix C: Exponents and scaling relations

When avalanches are well defined, the maximum avalanche size S_c is set by either temperature effects or finite size effects. In the case of finite size effects, the fractal dimension of avalanches enters, with $S_c \sim L^{d_f}$. Our

Exponent	Definition	Value (2d)	Value (mf)
τ	$p(S) \sim s^{-\tau} G(S/S_c)$	1.37 ± 0.07	1.5 ± 0.05
σ	$S_c \sim (\Delta\Sigma)^{-1/\sigma}$	1.05 ± 0.08	1.1 ± 0.06
θ	$p(x) \sim x^\theta$	0.52 ± 0.05	0.35 ± 0.03
n (athermal)	$\Sigma = \Sigma_c + C\dot{\gamma}^n$	0.67 ± 0.02	0.8 ± 0.02
n (thermal)	$\Sigma = \Sigma_c(T) + C\dot{\gamma}^n$	0.33 ± 0.06	0.4 ± 0.04
n (molten)	$\Sigma = \tau\mu\dot{\gamma}^n$	1 ± 0.01	1 ± 0.01

TABLE I. Numerically observed exponents for the thermal EPM model, with \pm errors representing acceptable fit ranges.

scaling description based on a simple truncated power-law for $p(x)$ finds that $d_f = d/((\theta + 1)(2 - \tau))$ in the athermal limit. When temperature effects are larger than finite-size effects, the maximum avalanche size scales as $s_c(T) \sim T^{-\theta/(\alpha(2-\tau))}$ or as $s_c \sim (\Delta\Sigma)^{-1/\sigma}$.

-
- [1] C. A. Schuh, T. C. Hufnagel, and U. Ramamurty, *Acta Materialia* **55**, 4067 (2007).
- [2] D. Bonn, M. M. Denn, L. Berthier, T. Divoux, and S. Manneville, *Reviews of Modern Physics* **89**, 035005 (2017), publisher: American Physical Society.
- [3] M. L. Manning, E. G. Daub, J. S. Langer, and J. M. Carlson, *Physical Review E* **79**, 016110 (2009), publisher: American Physical Society.
- [4] S. M. Fielding, *Reports on Progress in Physics* **77**, 102601 (2014), publisher: IOP Publishing.
- [5] S. M. Fielding, arXiv:2103.06782 [cond-mat] (2021), arXiv: 2103.06782.
- [6] A. S. Argon, *Acta Metallurgica* **27**, 47 (1979).
- [7] A. S. Argon and H. Y. Kuo, *Materials science and Engineering* **39**, 101 (1979).
- [8] C. E. Maloney and A. Lemaître, *Physical Review E* **74**, 016118 (2006), publisher: American Physical Society.
- [9] A. Nicolas, F. Puosi, H. Mizuno, and J.-L. Barrat, *Journal of the Mechanics and Physics of Solids* **78**, 333 (2015).
- [10] T. Albaret, A. Tanguy, F. Boioli, and D. Rodney, *Physical Review E* **93**, 053002 (2016).
- [11] A. Nicolas and J. Rottler, *Physical Review E* **97**, 063002 (2018).
- [12] J. Lin, E. Lerner, A. Rosso, and M. Wyart, *Proceedings of the National Academy of Sciences* **111**, 14382 (2014).
- [13] S. Sandfeld, Z. Budrikis, S. Zapperi, and D. F. Castellanos, *Journal of Statistical Mechanics: Theory and Experiment* **2015**, P02011 (2015).
- [14] E. A. Jagla, *Physical Review E* **92**, 042135 (2015).
- [15] C. Liu, E. E. Ferrero, F. Puosi, J.-L. Barrat, and K. Martens, *Physical review letters* **116**, 065501 (2016).
- [16] J. Lin and M. Wyart, *Physical review X* **6**, 011005 (2016).
- [17] Z. Budrikis, D. F. Castellanos, S. Sandfeld, M. Zaiser, and S. Zapperi, *Nature communications* **8**, 15928 (2017).
- [18] I. Fernández Aguirre and E. A. Jagla, *Physical Review E* **98**, 013002 (2018), publisher: American Physical Society.
- [19] E. E. Ferrero and E. A. Jagla, *Soft Matter* **15**, 9041 (2019), publisher: Royal Society of Chemistry.
- [20] E. E. Ferrero and E. A. Jagla, *Journal of Physics: Condensed Matter* **33**, 124001 (2021), publisher: IOP Publishing.
- [21] J. Lin, A. Saade, E. Lerner, A. Rosso, and M. Wyart, *EPL (Europhysics Letters)* **105**, 26003 (2014).
- [22] M. Le Goff, E. Bertin, and K. Martens, *Physical Review Letters* **123**, 108003 (2019), publisher: American Physical Society.
- [23] K. Karimi, E. E. Ferrero, and J.-L. Barrat, *Physical Review E* **95**, 013003 (2017).
- [24] K. M. Salerno, C. E. Maloney, and M. O. Robbins, *Physical review letters* **109**, 105703 (2012).
- [25] A. Nicolas, J.-L. Barrat, and J. Rottler, *Physical Review Letters* **116**, 058303 (2016).
- [26] K. M. Salerno and M. O. Robbins, *Physical Review E* **88**, 062206 (2013), publisher: American Physical Society.
- [27] A. Nicolas, E. E. Ferrero, K. Martens, and J.-L. Barrat, *Reviews of Modern Physics* **90**, 045006 (2018).
- [28] E. R. Homer and C. A. Schuh, *Acta Materialia* **57**, 2823 (2009).
- [29] Y. Shi and M. L. Falk, *Physical Review Letters* **95**, 095502 (2005), publisher: American Physical Society.
- [30] Y. Shi and M. L. Falk, *Physical Review B* **73**, 214201 (2006), publisher: American Physical Society.
- [31] H. J. Barlow, J. O. Cochran, and S. M. Fielding, *Physical Review Letters* **125**, 168003 (2020), publisher: American Physical Society.
- [32] S. Karmakar, E. Lerner, I. Procaccia, and J. Zylberg, *Physical Review E* **82**, 031301 (2010).
- [33] L. Bécu, S. Manneville, and A. Colin, *Physical Review Letters* **96**, 138302 (2006), publisher: American Physical Society.
- [34] M. Caggioni, V. Trappe, and P. T. Spicer, *Journal of Rheology* **64**, 413 (2020), publisher: The Society of Rheology.
- [35] J. Chatteraj, C. Caroli, and A. Lemaître, *Physical Review Letters* **105**, 266001 (2010), publisher: American Physical Society.
- [36] M. Popović, T. W. J. de Geus, W. Ji, and M. Wyart, *Phys. Rev. E* **104**, 025010 (2021).
- [37] E. E. Ferrero, A. B. Kolton, and E. A. Jagla, *Phys. Rev. Materials* **5**, 115602 (2021).
- [38] M. Popović, T. W. J. de Geus, W. Ji, A. Rosso, and M. Wyart, arXiv:2111.04061 [cond-mat] (2021), arXiv: 2111.04061.
- [39] S. Bustingorry, A. B. Kolton, and T. Giamarchi, *EPL (Europhysics Letters)* **81**, 26005 (2007), publisher: IOP Publishing.
- [40] C. E. Maloney and D. J. Lacks, *Physical Review E* **73**, 061106 (2006), publisher: American Physical Society.
- [41] D. G. Truhlar, B. C. Garrett, and S. J. Klippenstein, *The Journal of Physical Chemistry* **100**, 12771 (1996), publisher: American Chemical Society.
- [42] C. Ruscher and J. Rottler, *Soft Matter* **16**, 8940 (2020), publisher: The Royal Society of Chemistry.
- [43] C. Liu, S. Dutta, P. Chaudhuri, and K. Martens, *Physical Review Letters* **126**, 138005 (2021), publisher: American Physical Society.
- [44] B. Tyukodi, D. Vandembroucq, and C. E. Maloney, *Physical Review E* **100**, 043003 (2019).
- [45] J. T. Parley, S. M. Fielding, and P. Sollich, *Physics of Fluids* **32**, 127104 (2020), publisher: American Institute of Physics.
- [46] I. A. Gutowski, D. Lee, J. R. de Bruyn, and B. J. Frisken, *Rheologica Acta* **51**, 441 (2012).
- [47] D. Korchinski, C. Ruscher, and J. Rottler, *Physical Review E* **104**, 034603 (2021), publisher: American Physical Society.
- [48] H. G. E. Hentschel, S. Karmakar, E. Lerner, and I. Procaccia, *Physical Review Letters* **104**, 025501 (2010), publisher: American Physical Society.
- [49] J. Lin and M. Wyart, *Physical Review E* **97**, 012603 (2018).
- [50] J. Lin, T. Gueudré, A. Rosso, and M. Wyart, *Physical review letters* **115**, 168001 (2015).

- [51] S. Patinet, D. Vandembroucq, and M. L. Falk, *Physical Review Letters* **117**, 045501 (2016), publisher: American Physical Society.
- [52] A. Barbot, M. Lerbinger, A. Hernandez-Garcia, R. García-García, M. L. Falk, D. Vandembroucq, and S. Patinet, *Physical Review E* **97**, 033001 (2018), publisher: American Physical Society.
- [53] P. Virtanen, R. Gommers, T. E. Oliphant, M. Haberland, T. Reddy, D. Cournapeau, E. Burovski, P. Peterson, W. Weckesser, J. Bright, S. J. van der Walt, M. Brett, J. Wilson, K. J. Millman, N. Mayorov, A. R. J. Nelson, E. Jones, R. Kern, E. Larson, C. J. Carey, Í. Polat, Y. Feng, E. W. Moore, J. VanderPlas, D. Laxalde, J. Perktold, R. Cimrman, I. Henriksen, E. A. Quintero, C. R. Harris, A. M. Archibald, A. H. Ribeiro, F. Pedregosa, P. van Mulbregt, and SciPy 1.0 Contributors, *Nature Methods* **17**, 261 (2020).